NIPES - Journal of Science and Technology Research
www.nipes.org

Influence of Heat and Mass Generation on MHD Natural Convection Flow in a Vertical Concentric Annulus with Applied and Induced Magnetic Fields

MuhammadYusuf Muhammad [a*], Yusuf Ya'u Gambo [b] and Muhammad Auwal Lawan [c]

[a,c]Department of Mathematics, Aliko Dangote University of Science and Technology, Wudil Kano State Nigeria.

[b]Department of Mathematics, North West University Kano State Nigeria.

***Corresponding Author:** Muhammad Yusuf Muhammad, muhammadyusufmuhammad@kustwudil.edu.ng

Article Info

Keywords: *Magnetohydrodynamics (MHD), natural convection, vertical concentric annulus, heat generation, mass transfer, Hartmann number, Lorentz force, thermal transport.*

Received 03 February 2025
Revised 02 March 2025
Accepted 16 March 2025
Available online 25 April 2025

https://doi.org/10.37933/nipes/7.1.2025.23

eISSN-2682-5821, pISSN-2734-2352

Abstract

Conventional studies primarily focus on uniform or linear heat sources while often neglecting the effects of the induced magnetic field, leading to incomplete thermal and fluid flow characterizations. This study investigates the influence of inverse-square heat and mass generation on fully developed natural convection flow of an electrically conducting and viscous incompressible fluid, incorporating both applied and induced radial magnetic fields to provide a comprehensive understanding of their interplay. The governing equations of fluid motion, heat transfer, and induced magnetic fields are formulated in a non-dimensional form and analytically solved for velocity, temperature, concentration, magnetic field, and induced current density distributions alongside the numerical values of mass flux, induced current flux, Nusselt number and Sherwood number are presented in tabular form. The findings reveal that increasing the Hartmann number (Ha) suppresses velocity due to Lorentz force effects and resistive dissipation, while heat generation enhances fluid motion and alters temperature distribution. Larger annular spacing improves heat transfer efficiency, and variations in the chemical reaction parameter significantly affect concentration profiles. Additionally, induced current density fluctuations play a crucial role in electromagnetic control mechanisms. This study extends existing research by integrating applied and induced magnetic fields with a non-uniform heat and mass generation model, offering novel insights for optimizing MHD-based thermal management systems. The results provide a foundation for enhancing energy transport efficiency in nuclear reactors, geothermal energy systems, and high-performance electromagnetic applications.

1. Introduction

Magnetohydrodynamic (MHD) natural convection flow in a vertical concentric annulus has attracted significant attention due to its broad applications in engineering and industrial processes, such as nuclear reactor cooling, geothermal energy extraction, and space technology. The interaction between magnetic fields and convective heat and mass transfer plays a critical role in optimizing thermal management systems. The study and development of heat exchangers frequently involve annular configurations due to their extensive applications in various engineering and geophysical disciplines. These include magnetohydrodynamic (MHD) power systems, geothermal energy extraction, nuclear fuel debris processing, and the solidification of metals and alloys [1]. Natural convection around vertical cylindrical structures is employed in solar power absorption, geothermal extraction, and enhanced oil recovery. The presence of heat generation/absorption within a concentric annular space significantly improves fluid dynamics and the overall performance of thermal systems [2]. Magnetohydrodynamics (MHD), which integrates the principles of fluid dynamics and electromagnetism, allows for the regulation and movement of electrically conductive fluids through Lorentz forces generated by the interaction of electric currents and magnetic field.

In vertical concentric annuli, analyzing MHD-driven convection is essential for optimizing nuclear reactor cooling mechanisms, enhancing both safety and operational efficiency [3]. Furthermore, the effects of radial and induced magnetic fields have direct implications in geothermal energy systems and industrial processes, such as MHD propulsion and metal casting [4]. Heat generation and absorption play a crucial role in natural convection by modifying temperature gradients and flow behavior. These thermal effects are particularly significant in applications such as nuclear reactor cores, semiconductor fabrication, and combustion analysis. An radial variation of heat generation model provides a more realistic representation of heat transfer, addressing the limitations in existing studies that primarily consider uniform or linear heat sources [5]. Several researchers, including Smith and Johnson [6], as well as [7], have investigated the influence of radial magnetic fields on convective heat transfer and flow stability in annular geometries. Findings indicate that magnetic fields stimulate additional fluid motion, enhancing convective efficiency. For instance, Gupta and Sharma [8] demonstrated that radial magnetic fields decrease boundary layer thickness, thereby improving heat transfer near cylindrical walls. Neglecting the influence of induced magnetic fields has been shown to underestimate velocity and current density in MHD flows, underscoring its significance [9, 5, 10]. Understanding the interplay between radial and induced magnetic fields on fluid motion is essential for advancing technologies in metallurgy, nuclear fusion, and space exploration. These magnetic interactions dictate flow structures, turbulence behavior, and thermal transfer, facilitating precise regulation in nuclear reactor cooling systems and metal processing. In astrophysical contexts, they contribute to explaining plasma dynamics in solar flares and accretion disks. Additionally, a deeper comprehension of these effects improves plasma confinement in fusion reactors and refines computational MHD models, with applications extending to biomedical fields, including targeted drug delivery and medical imaging. The radially varying heat generation describes a scenario where heat absorption diminishes in proportion to the square of the distance from the heat source. This spatial dependence plays a crucial role in shaping temperature distributions and flow patterns within a system. Studies by [11] have examined the effects of heat absorption on MHD driven convection, highlighting its impact on transient free convection over vertical porous plates subjected to thermal radiation. Likewise, [12] explored the effects of heat generation and absorption in thermally stratified MHD flows over inclined stretching surfaces, demonstrating how absorption influences boundary layer temperature and velocity profiles. Further research into MHD convection, coupled with chemical reactions, has shown that heat absorption significantly alters concentration distributions, which is essential for mass transport processes [13]. Investigations into Joule heating and heat absorption in MHD nanofluid flows have also emphasized the role of absorption in either enhancing or diminishing heat transfer, depending on system configurations [14]. Another study focused on natural convection of a polar fluid within vertical annular spaces under transverse magnetic fields and Newtonian heating, providing insights for applications involving polar fluids in annular geometries [11]. Parameters such as the Hartmann number, annular spacing, and heat absorption parameters have been extensively examined in MHD studies. [15] reported that increased heat absorption leads to a decline in the Nusselt number, while another study [16] found that applying constant iso-flux heating modifies thermal energy distribution in vertical annuli. However, the combined effects of inverse-square heat absorption, radial magnetic fields, and induced magnetic fields on MHD-driven natural convection in vertical concentric annuli remain underexplored. [17] conducted research on MHD convection in a rectangular enclosure containing a trapezoidal heated obstacle and semi-circular wall heaters, using the finite element method to assess temperature and flow variations. Their results revealed that as the Hartmann number and buoyancy ratio increased, heat transfer on the right semicircular wall heater exceeded that of the left. Mathematical modeling and analytical solutions for predicting fluid behavior in such systems have garnered significant attention due to their industrial relevance. Many studies have examined natural convection within vertical annuli under various boundary conditions. [12] analyzed heat sources, sinks, and induced magnetic fields using theoretical models. Likewise, [18] studied heat absorption effects in natural convection along coaxial cylinders under constant iso-flux heating conditions. Additional works include research by [19] on laminar flow dynamics in open-ended [20] study on free convection in isothermal vertical annuli. Moreover, [21] presented analytical solutions for developing natural convection in vertical annuli under four distinct thermal boundary conditions. [22] further examined the role of induced magnetic fields in fully developed convection within annular micro-channels. Singh and Singh [23] examined free convective flow of electrically conducting fluid in vertical annular geometry when induced magnetic field is taken in to account in the presence of radial magnetic field. The behavior of electrically conductive fluids has attracted considerable attention for applications in battery technology and power generation. Foundational studies by Rossow [24] established theoretical frameworks, which were later expanded by researchers such as [25] [26] to explore MHD flows in coaxial cylinders under varying magnetic influences. Moalem [27] proposed that heat generation could be inversely related to temperature, a hypothesis that has been investigated in numerous studies focusing on heat generation and absorption in vertical concentric cylinders. The growing demand for advanced heat transfer solutions has driven research into heat-generating and heat-absorbing fluids. Earlier models assumed constant heat generation rates [28, 29], whereas recent studies have explored spatially varying heat sources and sinks [30, 22]. Investigations by Oni et al. [31] assessed the impact of radially varying magnetic fields and heat sources in vertical annular systems, contributing to a growing body of research in this field. Unlike previous studies that primarily considered uniform or linear heat sources, this study investigates inverse-square heat and mass generation and its impact on MHD convection. Furthermore, the inclusion of both applied and induced magnetic fields and make it double-diffusive convection model provides a more comprehensive analysis relevant to engineering applications. The current research seeks to fill existing gaps by examining how inverse-square heat and mass generation influences magnetohydrodynamic (MHD) natural convection within a vertical concentric annulus with induced and applied radial magnetic fields. Through analytical solutions of the governing equations, the research analyses the effects of key parameters which include the Hartmann number, heat generation parameter, and annular region on temperature profiles, velocity fields, induced magnetic density, and magnetic field distributions. The outcomes are pertinent to the optimization of MHD systems in engineering applications such as nuclear reactor cooling, geothermal energy extraction, and electromagnetic propulsion systems.

2. Mathematical Formulation

The configuration of the study as illustrated in Figure 1. We consider a fully developed natural convection flow of steady, viscous, incompressible electrically conducting fluid within a vertical concentric annulus of infinite length. The z' axis is oriented along the axis of coaxial cylinders is measured in the vertically upward direction, while R' represent the radial direction, measured outward from the axis of the cylinder. The applied magnetic field represented as $aH'_o/_{R'}$ is directed radial outward. The temperatures T'_i and T'_a denote the temperature at the outer surface of the inner cylinder and the ambient temperature, respectively ($T_i^{'} \geq T_a^{'}$) or at persistent rate $q^{'}$. The flow formation is in the domain $a \leq R^{'} \leq b$ of the annulus filled with heat generation. The velocity components are $U'_{R'}$, U'_θ and $U'_{z'}$, in the direction $R', \theta$and z' direction respectively. Since the flow is fully developed, then the velocity components $U'_{R'} = U'_\theta = 0$. The flow depends solely on R' due the fully developed nature and infinite length of the cylinders [18]. Exploring the Boussinesq approximation, the basic equations governing the flow for the model under study is obtained in dimensional form as (1), (2), (3), and (4).

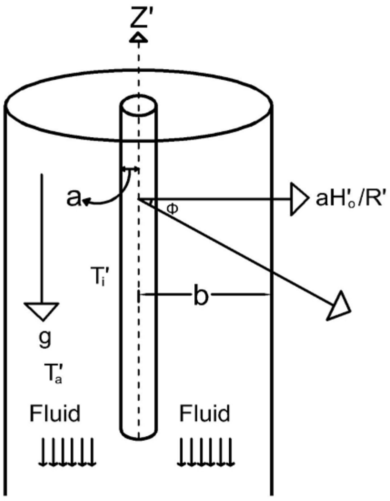

Figure 1: Geometry of the model [18].

$$\nu\left[\frac{1}{R'}\frac{d}{dR'}\left(R'\frac{dU'}{dR'}\right)\right]+g\beta(T'-T'_a)+g\beta^*(C^{'}-C^{'}_a)+\frac{a\mu_e H_o}{\rho R'}\frac{dH'_{z'}}{dR'}=0 \quad (1)$$

$$\eta\left[\frac{1}{R'}\frac{d}{dR'}\left(R'\frac{dH'_{z'}}{dR'}\right)\right]+\frac{aH'_0}{R'}\frac{dU'}{dR'}=0 \quad (2)$$

$$\frac{k}{\rho C_p}\left[\frac{1}{R'}\frac{d}{dR}\left(R'\frac{dT'}{dR'}\right)\right]+\frac{Q_o}{\rho C_p}=0 \quad (3)$$

$$D\left[\frac{1}{R^{'}}\frac{d}{dR^{'}}\left(R^{'}\frac{dC'}{dR^{'}}\right)\right]+K=0 \quad (4)$$

The boundary conditions for eqns. (1), (2), (3) and (4) are:

$$\begin{cases} U' = H'_{z'} = 0;\ C' = C'_i \,/\, \dfrac{dC'}{dR'} = -\dfrac{q^*}{D}, T' = T'_i \,/\, \dfrac{dT'}{dR'} = -\dfrac{q'}{k} \quad at\ R' = a \\ U' = H'_{z'} = 0; C' = C'_o, T' = T'_o \quad at\ R' = b \end{cases} \qquad (5)$$

In these equations, the following symbols represent various physical quantities: fluid velocity U', gravitational acceleration g, coefficient of volume expansion β, Magnetic permeability μ_e, fluid density ρ, magnetic diffusivity η, thermal conductivity of the fluid k, specific heat capacity at constant temperature C_p, fluid temperature T', fluid concentration C', reaction rate K'^*, diffusion coefficient D, ambient temperature T'_a, heat generation/absorption parameter respectively $Q_0 > 0$ and $Q_0 < 0$. Rendering equations (9)-(12) to the following non-dimensional variables and parameters we get (6), (7), (8), (9), and (10)

$$u = \frac{U'}{U_o},\ R = \frac{R'}{a},\ \theta = \frac{\left(T' - T'_a\right)}{\left(T'_i - T'_a\right)},\ H = \frac{H'_{z'}}{\sigma a \mu_e H'_o U_0},\ \lambda = \frac{b}{a},\ \phi = \frac{\left(C' - C'_a\right)}{\left(C'_i - C'_a\right)},\ (T'_i - T'_a) = \frac{q' a}{k}$$

$Q_o = \frac{Q_o^* a^2 (T' - T'_a)}{R'^2}$(radially-dependent heat generation function), $S = \frac{Q_o^* a^2}{k}$ (heat generation parameter),

$K = \frac{K' a^2 (C' - C'_a)}{R'^2}$ (radial dependent mass generation function), $K^* = \frac{K' a^2}{D}$ (chemical reaction parameter)

$N = \frac{\beta(T'_i - T'_a)}{\beta^*(C'_i - C'_a)}$(buoyancy ratio parameter), $U_o = \frac{g a^2 \beta (T'_i - T'_a)}{\nu}$ (Characteristic velocity),

, and $Ha = a\mu_e H'_o [\sigma/\rho\nu]^{\frac{1}{2}}$ (Hartmann number), we obtained the following dimensionless equations

$$\left[\frac{1}{R}\frac{d}{dR}\left(R\frac{du}{dR}\right)\right] + Ha^2\left[\frac{1}{R}\frac{dH}{dR}\right] + \theta + N\phi = 0 \quad (7)$$

$$\left[\frac{1}{R}\frac{d}{dR}\left(R\frac{dH}{dR}\right)\right] + \left[\frac{1}{R}\frac{du}{dR}\right] = 0 \qquad (8)$$

$$\left[\frac{1}{R}\frac{d}{dR}\left(R\frac{d\theta}{dR}\right)\right] + \frac{S}{R^2}\theta = 0 \qquad (9)$$

$$\left[\frac{1}{R}\frac{d}{dR}\left(R\frac{d\phi}{dR}\right)\right] + \frac{K^*}{R^2}\phi = 0 \qquad (10)$$

$$\begin{cases} u = H = 0;\ \chi\dfrac{d\phi}{dR} + \gamma\phi = \xi, \quad \chi\dfrac{d\theta}{dR} + \gamma\theta = \xi \quad at \quad R = 1 \\ u = H = 0;\ \phi = 0, \quad \theta = 0 \quad at \quad R = \lambda \end{cases} \qquad (11)$$

where $\chi, \gamma,$ and ξ are constants with χ=0, γ=1, $\xi = 1$ for isothermal and χ=1, γ=0, $\xi = -1$for iso-flux

3. Method

This study employs a methodology similar to that outlined in [18]. By applying non-dimensional boundary conditions, the dimensionless governing linear simultaneous ordinary differential equations are solved. The exact solutions for velocity, induced magnetic field, induced current density, concentration, and temperature fields are derived. Additionally, numerical values for skin friction, mass flux, induced current density, Sherwood number, and Nusselt number are computed to provide further insights into the system's behaviour.

3.1. Analytical solution

Solving equations (7)-(10), the velocity, skin friction, mass flux, magnetic field, induced current density, induced current flux, temperature, Nusselt number, concentration, Sherwood number were determined analytically, subject to boundary conditions (11) as follows:

$$u(R) = C_1 R^{Ha} + C_2 R^{-Ha} + C_3 + D_1 R^{(2+i\sqrt{S})} + D_2 R^{(2-i\sqrt{S})} + D_3 R^{(2+i\sqrt{K^*})} + D_4 R^{(2-i\sqrt{K^*})} \quad (12)$$

$$\tau_1 = \mathrm{Ha}(C_1 - C_2) + D_7 + D_8 \quad (13)$$

$$\tau_\lambda = -\mathrm{Ha}\left(C_1 \lambda^{\mathrm{Ha}-1} - C_2 \lambda^{-\mathrm{Ha}-1}\right) + D_9 + D_{10} \quad (14)$$

$$Q = 2\pi\left(\frac{C_1}{\mathrm{Ha}+2}(\lambda^{\mathrm{Ha}+2} - 1) + \frac{C_2}{2-\mathrm{Ha}}(\lambda^{2-\mathrm{Ha}} - 1) + D_{16}\right) \quad (15)$$

$$H(R) = C_4 + C_3 \ln(R) - \frac{C_1}{Ha} R^{Ha} + \frac{C_2}{Ha} R^{-Ha} - \frac{D_1}{2+\sqrt{S}} R^{2+i\sqrt{S}} - \frac{D_2}{2-\sqrt{S}} R^{2-i\sqrt{S}} - \frac{D_3}{2+\sqrt{K^*}} R^{2+i\sqrt{K^*}} - \frac{D_4}{2-\sqrt{K^*}} R^{2-i\sqrt{K^*}} \quad (16)$$

$$J_\theta = C_1 R^{Ha-1} + C_2 R^{-Ha-1} + D_1 R^{1+i\sqrt{S}} + D_2 R^{1-i\sqrt{S}} + D_3 R^{1+i\sqrt{K^*}} + D_4 R^{1-i\sqrt{K^*}} - \frac{C_3}{R} \quad (17)$$

$$J = \frac{1}{Ha}\Big(C_1(\lambda^{Ha} - 1) - C_2(\lambda^{-Ha} - 1)\Big) + D_{24} + D_{25} \quad (18)$$

$$\theta(R) = \frac{\xi\left[R^{2i\sqrt{S}} - \lambda^{2i\sqrt{S}} R^{-i\sqrt{S}}\right]}{\left(\chi i\sqrt{S} + \gamma\right) + \left(\chi i\sqrt{S} - \gamma\right)\lambda^{2i\sqrt{S}}} \quad (19)$$

$$\tau_1 = \frac{d\theta}{dR}\Big|_{R=1} = -i\sqrt{S}\left(C_5 - C_6\right) \quad (20)$$

$$\tau_\lambda = -\frac{d\theta}{dR}\Big|_{R=\lambda} = -i\sqrt{S}\left(C_5 \lambda^{i\sqrt{S}-1} - C_6 \lambda^{-i\sqrt{S}-1}\right) \quad (21)$$

$$\Phi(R) = \frac{\xi\left[R^{2i\sqrt{K^*}} - \lambda^{2i\sqrt{K^*}} R^{-i\sqrt{K^*}}\right]}{\left(\chi i\sqrt{K^*} + \gamma\right) + \left(\chi i\sqrt{K^*} - \gamma\right)\lambda^{2i\sqrt{K^*}}} \quad (22)$$

$$Sh_1 = \frac{d\theta}{dR}\Big|_{R=1} = -i\sqrt{K^*}\left(C_5 - C_6\right) \quad (23)$$

$$Sh_\lambda = -\frac{d\theta}{dR}\Big|_{R=\lambda} = -i\sqrt{K^*}\left(C_5 \lambda^{i\sqrt{K^*}-1} - C_6 \lambda^{-i\sqrt{K^*}-1}\right) \quad (24)$$

The constants in the equations (17)-(26) are given in Appendix 1.

4. Results

To analyse the fluid flow characteristics, the governing equations were solved analytically, and the outcomes were illustrated using MATLAB-generated plots. This investigation centred on three critical parameters: heat generation parameter (S), radii ratio (λ), and Hartmann number (Ha). Each parameter was systematically varied while holding the others constant to examine its individual impact, as reflected in Figures 1 through 27. Numerical data corresponding to equations (13), (14), (15), (18), (20), (21), (22) and (25) are presented in Tables 4 and 5. The Hartmann number was explored across a range consistent with prior research, including studies by [1], [31], [18] and [23]. The observed variations in thermal, concentration, velocity, magnetic field, and induced current density profiles under varying parametric conditions as depicted in Figures 1 to 27, highlight their dependence and the influence of key dimensionless parameters on the annular region (λ), heat generation parameter (S), chemical reaction parameter (K^*), Hartmann number (Ha), and buoyancy ratio (N), under both isothermal and iso-flux boundary conditions.

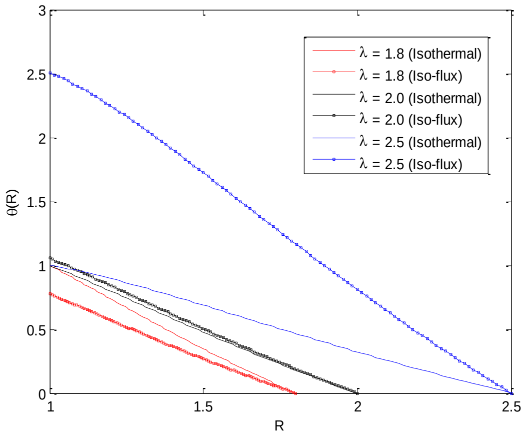

Figure 1: Temperature profile for different values of λ at S=2

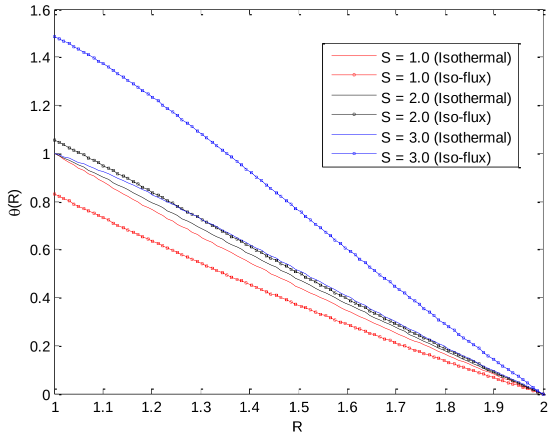

Figure 2: Temperature profile for different values of S at λ=2

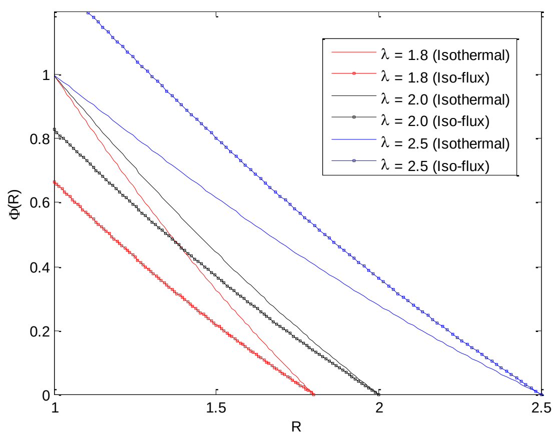

Figure 3: Concentration profile for different values of λ at $K^* = 0.5$

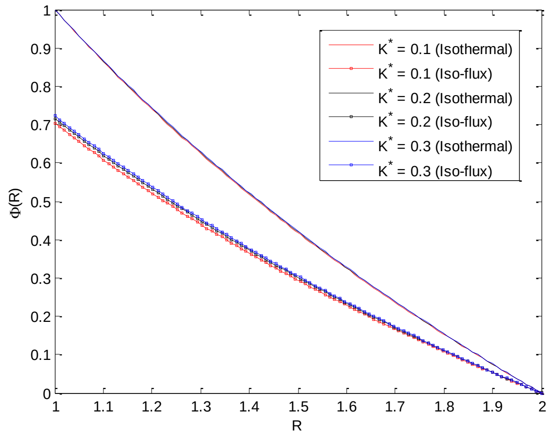

Figure 4: Concentration profile for different values of K^* at $\lambda = 1$.

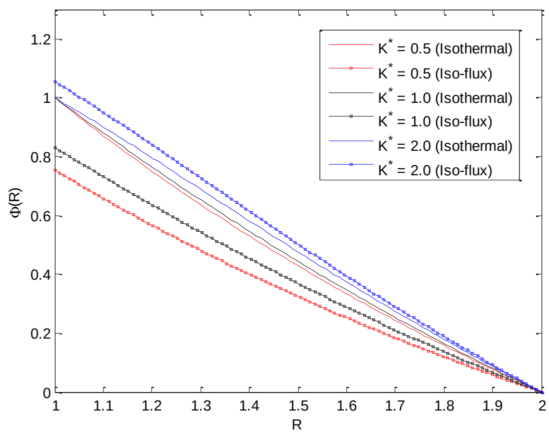

Figure 5: Concentration profile for different values of K^*at $\lambda = 2$.

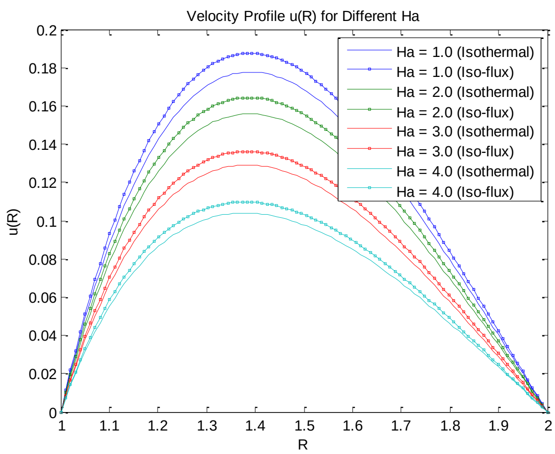

Figure 6: Velocity profile for different values for Ha at $K^* = 1, S = 2, N = 2$ and $\lambda = 2$.

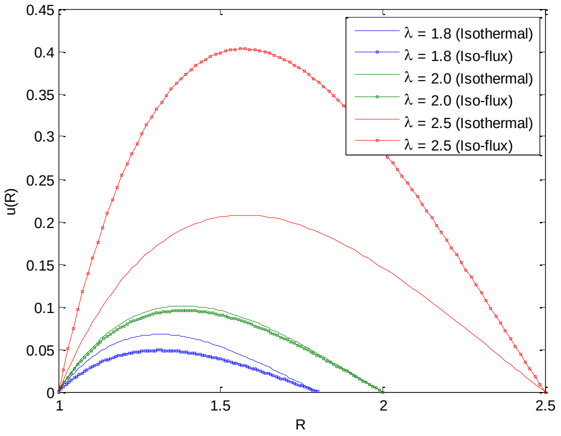

Figure 7: Velocity profile for different values for lambda at $K^* = 1, S = 2, N = 1$ and $Ha = 2$.

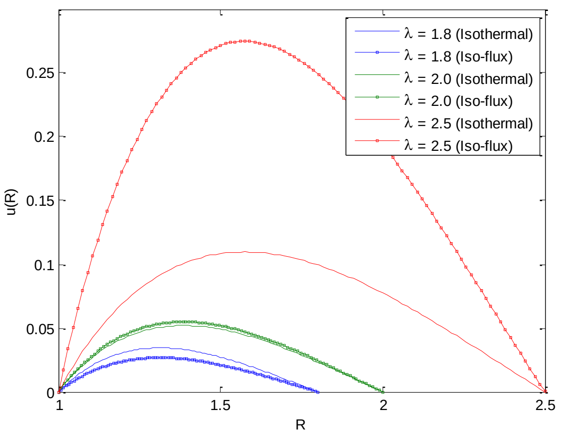

Figure 8: Velocity profile for different values for lambda at $S = 2, N = 1, Ha = 2$ and $K^* \to 0$

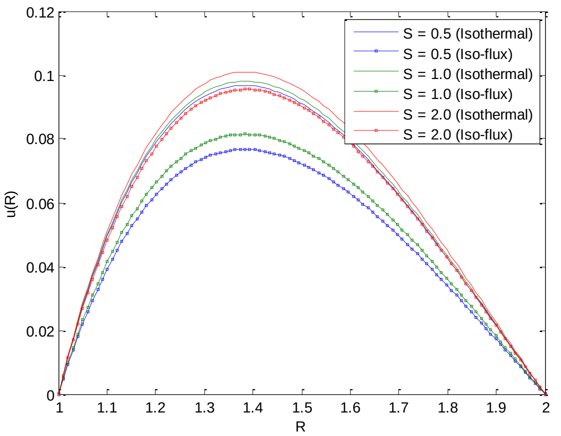

Figure 9: Velocity profile for different values for S at $K^* = 1, \lambda = 2$, N=1 and Ha=2

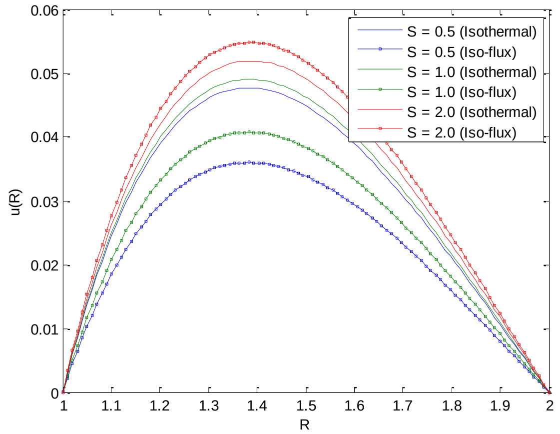

Figure 10: Velocity profile for different values for S at $\lambda = 2$, N=1, Ha=2 and $K^* \to 0$,

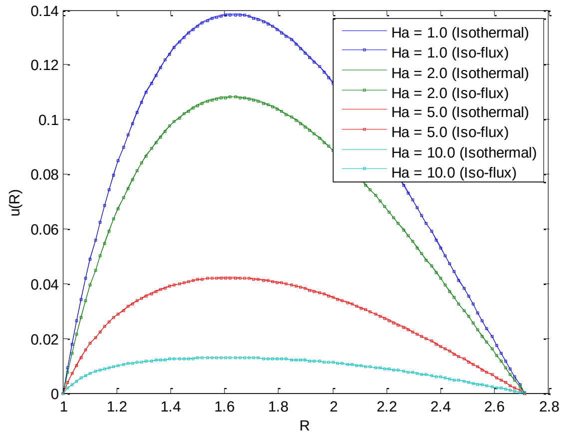

Figure 11: Velocity profile for different values for Ha at $\lambda = 2.71$, N=0, $K^* \to 0$, and $S \to 0$, Which is similar to study of (Singh & Singh, [23])

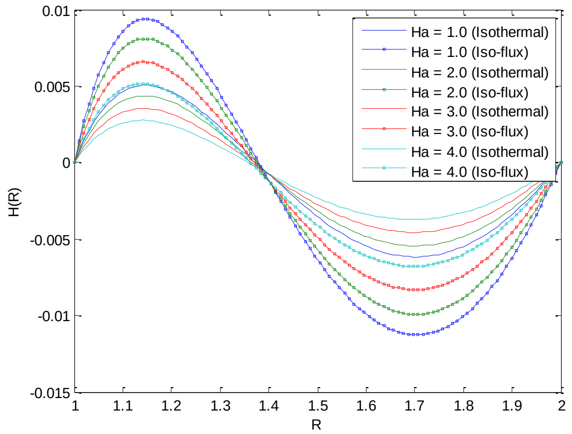

Figure 12: Magnetic profile for different values of Ha at $\lambda = 2, K^* = 1$, N=1 and S=4

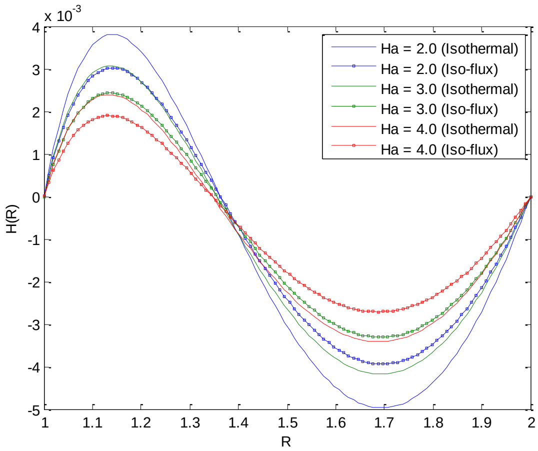

Figure 13: Magnetic profile for different values of Ha at $\lambda = 2$, $K^* = 1$, N=1 and S=0.5

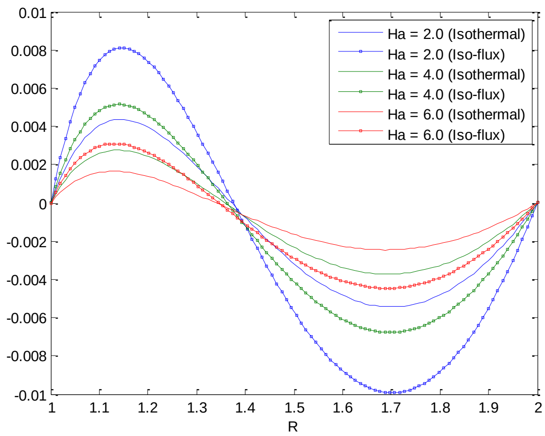

Figure 16: Magnetic profile for different values of Ha at $\lambda = 2$, $K^* = 1$, N=1 and S=4

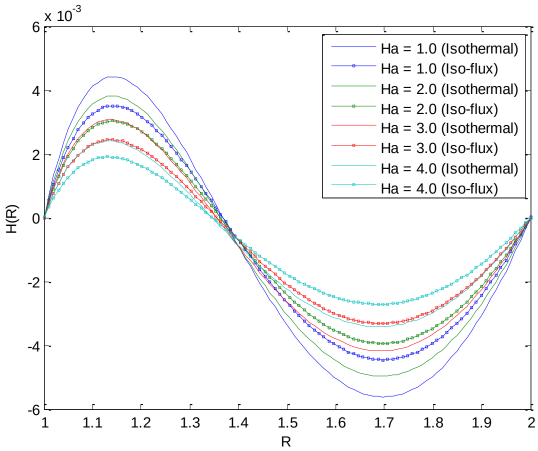

Figure 14: Magnetic profile for different values of Ha at $\lambda = 2$, $K^* = 1$, N=1 and S=0.5

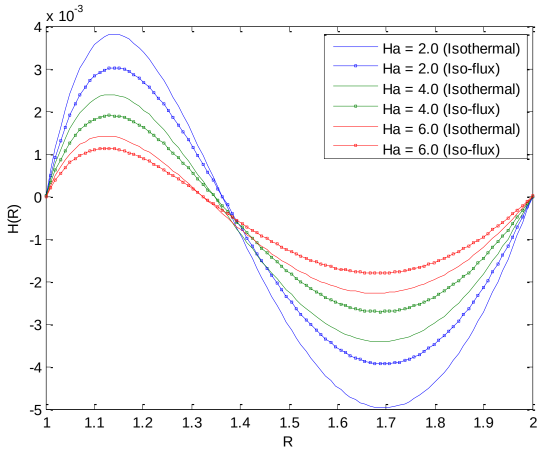

Figure 17: Magnetic profile for different values of Ha at $\lambda = 2$, $K^* = 1$, N=1 and S=0.5

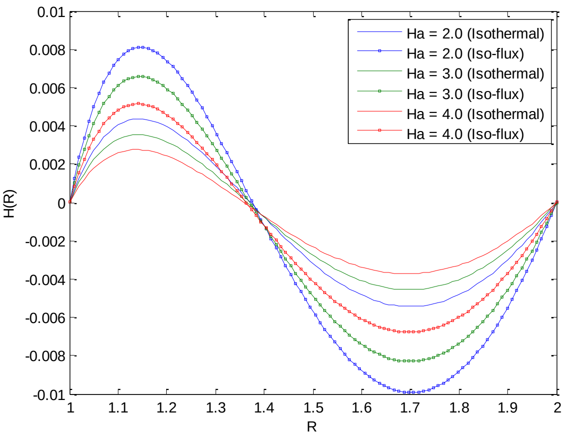

Figure 15: Magnetic profile for different values of Ha at $\lambda = 2$, $K^* = 1$, N=1 and S=4

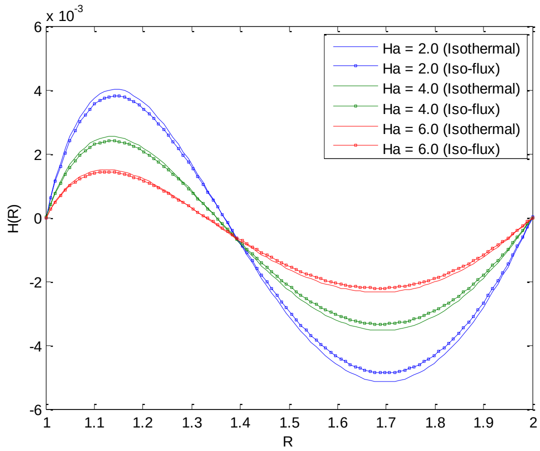

Figure 18: Magnetic profile for different values of Ha at $\lambda = 2$, $K^* = 1$, N=1 and S=2

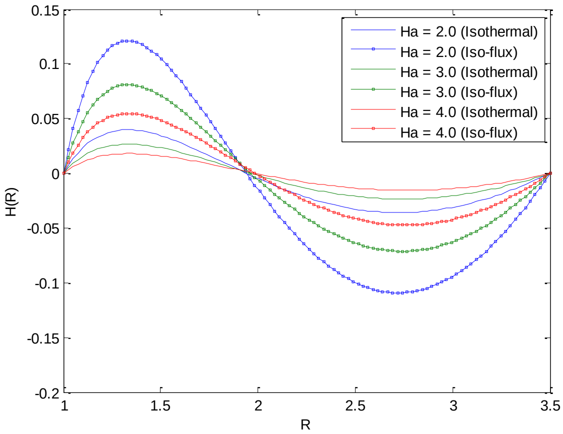

Figure 19: Magnetic profile for different values of Ha at $\lambda = 3.5$, $K^* = 1$, N=1 and S=1

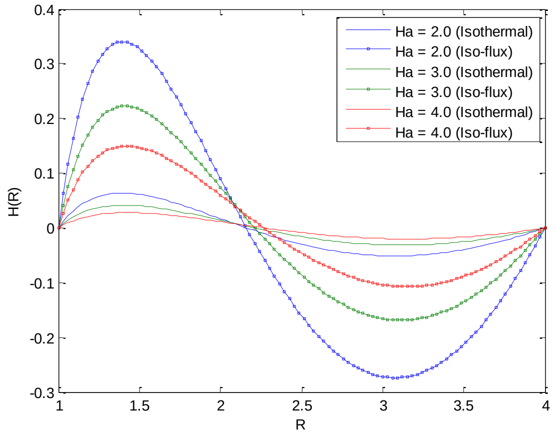

Figure 20: Magnetic profile for different values of Ha at $\lambda = 4$, $K^* = 1$, N=1 and S=1

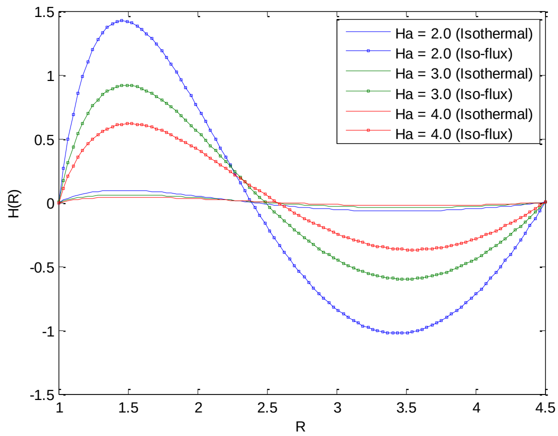

Figure 21: Magnetic profile for different values of Ha at $\lambda = 4.5$, $K^* = 1$, N=1 and S=1

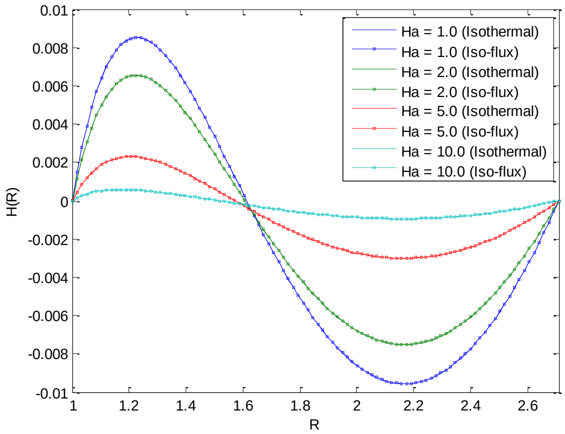

Figure 22: Magnetic profile for different values of Ha at $\lambda = 2.71$, N=0, $K^* \to 0$ and $S \to 0$ Which is similar to the study of (Singh & Singh, [23])

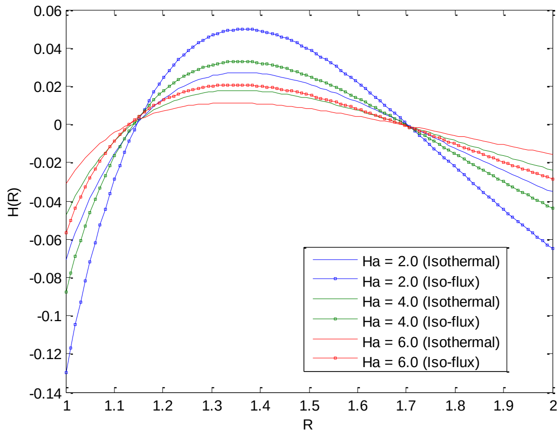

Figure 23: Induced current density profile for different values of Ha at $\lambda = 4$, $K^* = 1$, N=1 and S=4

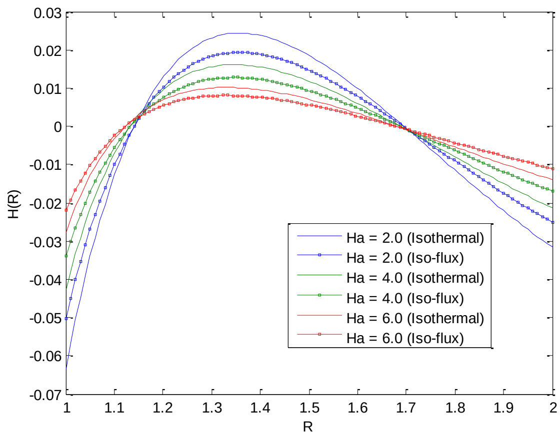

Figure 24: Induced current density profile for different values of Ha at $\lambda = 4$, $K^* = 1$, N=1 and S=0.5

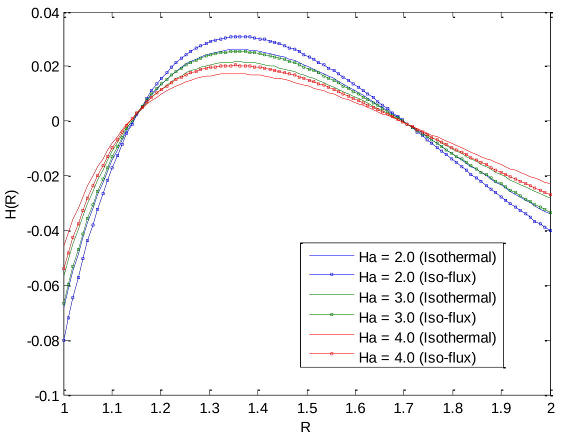

Figure 25: Induced current density profile for different values of Ha at $\lambda = 4$, $K^* = 1$, N=1 and S=3

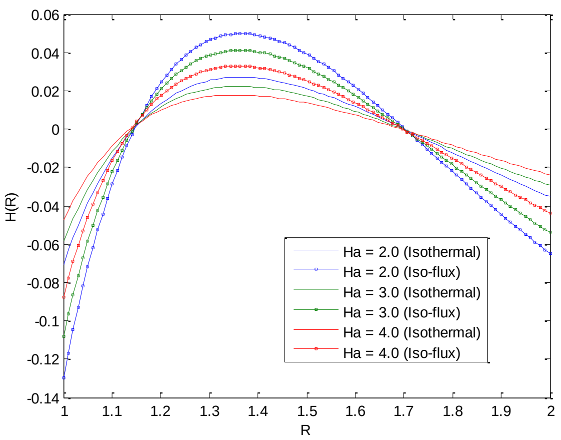

Figure 26: Induced current density profile for different values of Ha at $\lambda = 4$, $K^* = 1$, N=1 and S=4

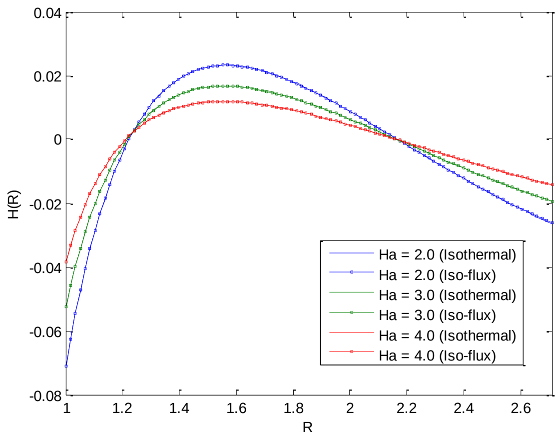

Figure 27: Induced current density profile for different values of Ha at $\lambda = 2.71$, N=0, $K^* =\to 0$ and $S \to 0$ which is similar to the study of (Singh & Singh, [23]).

5. **Discussion**

Table 1 reveals that as Ha increases, skin friction decreases in both isothermal and iso-flux cases, indicating a reduction in shear stress at the cylinder wall. This is due to the stronger magnetic field suppressing fluid motion. Also, an increase in λ leads to higher skin friction, suggesting that a wider annular space results in greater shear stress. Additionally, a slight increase in skin friction is observed with rising$S$, implying that higher heat generation enhances thermal buoyancy, thereby influencing velocity-gradients.

Table 2 shows that the induced current flux (J), fluctuates between positive and negative values as Ha increases. For larger λ, induced current flux exhibits greater variability, highlighting the influence of the annular gap on the fluid-magnetic field interaction. Similarly, increasing S affects the magnitude of the induced current density, further demonstrating the role of heat generation in altering electromagnetic properties. Table 4 presents the induced current density for varying K^*. Significant variations in J with changes in K^*. suggest that the chemical reaction parameter strongly influences the behavior of the electrically conducting fluid. Table 5 provides Nusselt numbers for both the inner and outer cylinders. As λ increases, Nusselt number (Nu) decreases, indicating reduced convective heat transfer efficiency. Conversely, higher values of S lead to an increase in Nusselt number, confirming that heat generation enhances thermal transport. Notably, Nusselt number is higher under isothermal conditions than in iso-flux cases, suggesting that maintaining a fixed temperature difference improves heat transfer efficiency. Finally, Table 6 presents the Sherwood number (Sh). As λ increases, Sh decreases, signifying reduced mass transfer efficiency. Large values of K^* result in significant changes in Sh, indicating that chemical reactions strongly influence concentration gradients and mass flux. Similar to the Nusselt number, Sh is higher under isothermal conditions, reinforcing the notion that a fixed concentration difference enhances mass transport.

Figures 1 and 2 illustrate the temperature profile θ(R) as a function of the annular gap (λ) and heat generation parameter (S), respectively. As λ increases, the temperature distribution becomes more uniform, indicating improved thermal regulation due to enhanced convective heat transfer The iso-flux boundary condition consistently exhibits a steeper temperature gradient than the isothermal case, highlighting the continuity of heat flux at the boundary. The increase in S results in a proportional rise in temperature, signifying stronger internal heat generation and its pronounced effect on thermal conductivity. Figures 3–5 depict the concentration profile θ(R) for different values of λ and K^*. The results indicate that lower λ values correspond to steeper concentration gradients, which suggest a higher diffusion rate. The iso-flux condition produces a flatter concentration profile than the isothermal case, reinforcing the role of boundary constraints in diffusion processes.

Table 1: Numerical values of skin friction for both isothermal and iso-flux condition for different values of Ha, λ, and S at N=0.75 and K*=1.

			Isothermal			**Iso-flux**		
Λ	Ha	S	τ_1	τ_λ	Q	τ_1	τ_λ	Q
1.8	0.5	0.5	0.47894	0.18146	0.28485	0.30766	0.11658	0.18300
1.8	1	0.5	0.46963	0.17663	0.27758	0.30168	0.11348	0.17833
1.8	1.5	0.5	0.45509	0.16911	0.26626	0.29234	0.10865	0.17106
1.8	2	0.5	0.43650	0.15956	0.25184	0.28040	0.10251	0.16179
2	0.5	0.5	0.60543	0.21899	0.58368	0.47680	0.17251	0.45976
2	1	0.5	0.58882	0.21114	0.56326	0.46372	0.16633	0.44368
2	1.5	0.5	0.56350	0.19922	0.53221	0.44377	0.15694	0.41922
2	2	0.5	0.53218	0.18456	0.49399	0.41910	0.14539	0.38912
3	0.5	0.5	1.29607	0.39562	5.86194	2.12774	0.65111	9.64135
3	1	0.5	1.20310	0.36474	5.38637	1.97491	0.60031	8.85930
3	1.5	0.5	1.07762	0.32309	4.74565	1.76866	0.53180	7.80566
3	2	0.5	0.94454	0.27897	4.06809	1.54993	0.45923	6.69140
1.8	0.5	1	0.48270	0.18377	0.28807	0.32165	0.12246	0.19196
1.8	1	1	0.47329	0.17889	0.28073	0.31538	0.11920	0.18706
1.8	1.5	1	0.45859	0.17128	0.26928	0.30559	0.11414	0.17944
1.8	2	1	0.43981	0.16162	0.25470	0.29307	0.10769	0.16972
2	0.5	1	0.61229	0.22297	0.59315	0.50859	0.18521	0.49270
2	1	1	0.59543	0.21499	0.57240	0.49459	0.17858	0.47546
2	1.5	1	0.56973	0.20287	0.54086	0.47324	0.16851	0.44926
2	2	1	0.53795	0.18797	0.50203	0.44684	0.15613	0.41701
3	0.5	1	1.33935	0.41549	6.13122	2.62250	0.81355	12.0051
3	1	1	1.24246	0.38319	5.63435	2.43278	0.75030	11.0323
3	1.5	1	1.11173	0.33961	4.96489	2.17681	0.66497	9.72142
3	2	1	0.97315	0.29343	4.25685	1.90547	0.57454	8.33506

Table 2: Numerical values of induced current flux for both isothermal and iso-flux condition for different values of Ha, λ, and S at N=0.75 and K*=1.

			Isothermal	**Iso-flux**
Ha	S	λ	$J/10^{-16}$	$J/10^{-16}$
1	0.5	1.8	5.5511	-3.3306
1.5	0.5	1.8	-3.3306	-2.2204
2	0.5	1.8	5.5511	1.6653
0.5	0.5	2	-8.8817	-1.2212
1	0.5	2	0.0000	-4.4408
1.5	0.5	2	1.1102	-3.3306
2	0.5	2	5.5511	1.6653
0.5	0.5	3	-2.2204	5.1070
1	0.5	3	3.3306	-1.1102
1.5	0.5	3	4.4408	-6.6613
2	0.5	3	-3.3306	-2.2204
0.5	1	1.8	1.6653	6.6613
1	1	1.8	-1.1102	-3.3306
1.5	1	1.8	3.3306	0.0000
2	1	1.8	-1.1102	-1.1102
0.5	1	2	-7.2164	-5.5511
1	1	2	-2.2204	2.2204
1.5	1	2	3.3306	0.0000
2	1	2	1.1102	1.1102
0.5	1	3	2.2204	-3.3306
1	1	3	5.5511	2.4424
1.5	1	3	0.0000	-2.2204
2	1	3	-1.1102	6.6613

Notably, an increase in K^* leads to more uniform concentration distributions, implying improved mass transport efficiency and reaction kinetics. The velocity profile $u(R)$ is analyzed in Figures 6–11 for variations in the Hartmann number (Ha), annular gap (λ), and heat generation parameter (S). As Ha increases, velocity decreases due to the Lorentz force-induced magnetic damping effect, which suppresses fluid motion. The iso-flux condition exhibits smoother velocity profiles, indicating a more controlled fluid motion. Furthermore, larger λ values enhance fluid motion by reducing flow resistance, promoting efficient transport. The increase in S leads to accelerated flow dynamics, as stronger thermal sources enhance convective effects and momentum transfer within the fluid. Figures 12–22 examine the influence of the Hartmann number (Ha) on the magnetic field profile $H(R)$. Increasing Ha results in stronger magnetic interactions, particularly near the boundaries, due to intensified electromagnetic coupling. Iso-flux conditions consistently produce smoother magnetic field variations compared to isothermal cases, demonstrating the impact of thermal constraints. Furthermore, the heat generation parameter S plays a crucial role in modulating magnetic field intensity, as higher S values amplify magnetic effects and influence the stability of the MHD system. Induced magnetic fields generate. The secondary flow instabilities by modifying current density gradients could lead to localized variations in temperature and velocity, impacting the stability and efficiency of MHD systems in practical engineering applications such as nuclear reactor cooling and electromagnetic propulsion. Figures 23–27 present the induced current density profile $J_\theta(R)$ for different Ha values. The results reveal that increasing Ha enhances current density near the boundaries due to stronger electromagnetic interactions. However, at lower S values, the induced current density diminishes, indicating reduced thermal-electromagnetic coupling. The findings align with previous studies, validating the theoretical models governing MHD flow and providing critical insights for optimizing electromagnetic fluid control in engineering applications.

Table 4: Numerical values of induced current flux for both isothermal and iso-flux condition for different values of Ha, λ, and K* at N=0.75 and S=1.

			Isothermal	**Iso-flux**
Ha	K*	**Λ**	$J/10^{-16}$	$J/10^{-16}$
0.5	0.4	1.8	16.653	9.9926
1	0.4	1.8	-7.7715	-4.4408
1.5	0.4	1.8	1.1102	-0.5551
2	0.4	1.8	0.0000	-4.4408
0.5	1	1.8	1.6653	6.6613
1	1	1.8	-1.1102	-3.3306
1.5	1	1.8	3.3306	0.0000
2	1	1.8	-1.1102	-1.1102
0.5	0.4	2	19.984	0.0000
1	0.4	2	-5.5511	1.6653
1.5	0.4	2	-2.2204	0.0000
2	0.4	2	0.0000	0.0000
0.5	1	2	-7.2164	-5.5511
1	1	2	-2.2204	2.2204
1.5	1	2	3.3306	0.0000
2	1	2	1.1102	1.1102
0.5	0.4	3	-2.2204	-1.5543
1	0.4	3	2.2204	4.4408
1.5	0.4	3	-2.2204	4.4408
2	0.4	3	0.0000	0.0000
0.5	1	3	2.2204	-3.3306
1	1	3	5.5511	2.4424
1.5	1	3	0.0000	-2.2204
2	1	3	-1.1102	6.6613

Table 5: Numerical Dimensionless Nusselt Number for Both Isothermal and Iso-flux Conditions.

		Isothermal		**Iso-flux**	
λ	S	Nu_1	Nu_λ	Nu_1	Nu_λ
1.8	1	1.5007	1.0019	1.0000	0.6676
2	1	1.2039	0.7825	1.0000	0.6500
2.5	1	0.7673	0.5042	1.0000	0.6571
1.8	2	1.2901	1.0635	1.0000	0.8243
2	2	0.9480	0.8513	1.0000	0.8980
2.5	2	0.3990	0.5878	1.0000	1.4732

Table 6: Numerical Dimensionless Sherwood Number for Both Isothermal and Iso-Flux Conditions.

		Isothermal		**Iso-flux**	
Λ	K*	Sh_1	Sh_λ	Sh_1	Sh_λ
1.8	0.4	1.6222	0.9673	1.0000	0.5963
2	0.4	1.3491	0.7450	1.0000	0.5522
2.5	0.4	0.9664	0.462	1.0000	0.4781
1.8	1	1.5007	1.0019	1.0000	0.6676
2	1	1.2039	0.7825	1.0000	0.6500
2.5	1	0.7673	0.5042	1.0000	0.6571

Table 7: Comparison of Numerical values of fluid flux for isothermal and constant heat flux cases of this study and the study of Singh and Singh [23] at $S \to 0$, $K^* = 0$ and $N = 0$

		Existing study [23]		**Current study**	
λ	M	Q (isothermal)	Q (iso-flux)	Q (isothermal)	Q (iso-flux)
1.8	0.5	0.15943	0.09371	0.15828	0.09304
1.8	1	0.15874	0.09331	0.15424	0.09067
1.8	1.5	0.15761	0.09264	0.14795	0.08697
1.8	2	0.15610	0.09174	0.13993	0.08226
2	0.5	0.32375	0.22441	0.32050	0.22219
2	1	0.32181	0.22306	0.30928	0.21441
2	1.5	0.31865	0.22087	0.29222	0.20258
2	2	0.31437	0.21790	0.27122	0.18803
3	0.5	3.07501	3.37825	2.99970	3.29683
3	1	3.02972	3.32849	2.75564	3.02860
3	1.5	2.95830	3.25003	2.42690	2.66730
3	2	2.86598	3.14860	2.07935	2.28532
4	0.5	11.9607	16.5811	11.51038	15.96701
4	1	11.6868	16.2013	10.1314	14.05411
4	1.5	11.2679	15.6206	8.45293	11.72577
4	2	10.7484	14.9005	6.86807	9.52728

5. 1. Comparison and Validation

Table 8: Comparison of Numerical values of skin friction for isothermal and constant heat flux cases of this study and the study of [23] at $S \to 0$, $K^* = 0$ and $N = 0$

		Current study				Existing study [23]			
Λ	M	τ_1 (isothermal)	τ_1 (iso-flux)	τ_λ (isotherm)	τ_λ (iso-flux)	τ_1 (isothermal)	τ_1 (iso-flux)	τ_λ (isothermal)	τ_λ (iso-flux)
1.8	0.5	0.26844	0.15781	0.10047	0.05906	0.27016	0.1588	0.10142	0.05962
1.8	1	0.26326	0.15476	0.09779	0.05749	0.26998	0.15869	0.10152	0.05967
1.8	1.5	0.25516	0.15000	0.09361	0.05503	0.26969	0.15852	0.10169	0.05977
1.8	2	0.24481	0.14391	0.08831	0.05191	0.26929	0.15829	0.10191	0.05990
2	0.5	0.33650	0.23328	0.11967	0.08296	0.33959	0.23539	0.12122	0.08402
2	1	0.32735	0.22694	0.11536	0.07998	0.33932	0.23520	0.12135	0.08411
2	1.5	0.31340	0.21727	0.10882	0.07544	0.33889	0.23400	0.12156	0.08426
2	2	0.29615	0.20531	0.10078	0.06987	0.33831	0.23450	0.12186	0.08447
3	0.5	0.68409	0.75185	0.20030	0.22014	0.70185	0.77106	0.20621	0.22655
3	1	0.63607	0.69908	0.18450	0.20278	0.70154	0.77072	0.20631	0.22666
3	1.5	0.57121	0.62779	0.16321	0.17937	0.70104	0.77018	0.20648	0.22684
3	2	0.50232	0.55208	0.14068	0.15461	0.70040	0.76947	0.20669	0.22708
4	0.5	1.04426	1.44858	0.26680	0.37010	1.09111	1.51260	0.27849	0.38606
4	1	0.92740	1.28647	0.23687	0.32858	1.09254	1.51458	0.27813	0.38557
4	1.5	0.78540	1.08950	0.20029	0.27784	1.09470	1.51757	0.27759	0.38482
4	2	0.65161	0.90391	0.16552	0.22961	1.09732	1.52121	0.27693	0.38391

Table 7 and 8 depict the comparison between the current study and Singh & Singh [23] for the numerical values for mass flux (Q), skin friction (τ_1) and (τ_λ) at the inner and outer cylinder surfaces, respectively, for both cases. The values for τ_1, and τ_λ are generally consistent across both studies, with only minor deviations. This agreement confirms the validity of both approaches in evaluating the influence of the Hartmann number M and the annular gap λ on skin friction. Small numerical differences (on the order of ~1–2%) exist between the two studies for some values, likely due to variations in numerical methods or precision and also, due to Slight differences in boundary condition implementations.

5.2. Validation of Findings: Both studies demonstrate consistent trends in the behavior of skin friction and mass flux with changes in M and λ, validating the results.

Table 9: summarizing how the current study improves upon the existing research [23]

Aspect	**Current Study**	**Existing Study [23]**	**Improvement/Novelty**
Problem Focus	MHD natural convection flow in a vertical concentric annulus with heat and mass generation.	MHD natural convection in vertical concentric annuli with a radial magnetic field.	Incorporates heat and mass generation effects.
Momentum Equation	Include solutal buoyancy	No solutal buoyancy	Making it a double-diffusive convection model
Mathematical Approach	Analytical solutions for velocity, temperature, concentration, and induced current density.	Analytical solutions for velocity, induced magnetic field, and temperature.	Includes additional transport phenomena (mass transport).
Heat & Mass Transfer	Includes radially varying heat and mass generation	No heat generation purely heat conduction in the medium	More realistic thermal modeling for industrial applications
Boundary Conditions	Both isothermal, iso-flux, fixed concentration, and constant mass flux conditions on the inner cylinder.	Isothermal and constant heat flux boundary conditions.	More generalized thermal boundary conditions.
Parametric Analysis	Hartmann number (Ha), heat generation (S), chemical reaction (K*), annular gap (λ), and buoyancy ratio (N*).	Hartmann number (M), annular gap (λ), and induced magnetic field effects.	Includes chemical reaction and heat generation effects.
Heat and Mass Transfer	Examines Nusselt number, Sherwood number, and mass flux under different conditions.	Focuses on temperature and velocity profiles without considering mass transfer effects.	Extends analysis to mass transport.
Numerical Simulations	Graphical and tabular analysis of multiple parameters, validating analytical solutions.	Graphical analysis of velocity and magnetic field effects.	More comprehensive parametric study with additional physical quantities.
Applications	Relevant to nuclear reactor cooling, geothermal energy extraction, and electromagnetic propulsion.	Heat exchangers, nuclear fuel processing, and MHD power generators.	Expands application scope to include chemical and mass transport phenomena.

This study builds upon Singh & Singh [23] by incorporating radially-varying heat and mass generation, analyzing additional physical effects, and providing a more detailed parametric investigation.

6. Conclusion

This study presents analysis of MHD natural convection flow in a vertical concentric annulus with radius square inverse heat and mass generation subjected to isothermal and iso-flux heating. The key findings are summarized as follows:

Increasing Ha suppresses velocity due to the Lorentz force, which dampens fluid motion. The magnetic field intensity increases with Ha, leading to stronger electromagnetic interactions.

Higher heat generation (S) enhances fluid velocity and temperature distribution. Increasing S improves convective heat transfer but also affects the stability of the system.

Larger annular spacing promotes fluid motion by reducing flow resistance. Temperature distribution becomes more uniform with increasing λ, improving thermal regulation. Chemical reaction parameter affects concentration distribution significantly, influencing mass transfer efficiency. Higher (K^*) leads to more uniform concentration profiles, reducing diffusion gradients.
Induced current density increases with Ha due to stronger electromagnetic interactions. Higher λ and S influence the induced current flux, demonstrating the role of thermal and mass transport in altering electromagnetic properties.
Skin friction decreases with increasing Ha, indicating lower shear stress due to magnetic damping.
Nusselt number decreases with increasing λ, showing reduced convective heat transfer. Sherwood number also decreases with λ, suggesting lower mass transfer efficiency at larger annular gaps.
Results are consistent with prior research (e.g., [23]), validating the analytical findings. The study provides a more detailed investigation of the combined effects of radial and induced magnetic fields. Findings are relevant for optimizing MHD systems used in nuclear reactor cooling, geothermal energy extraction, and electromagnetic propulsion. Also, insights into heat and mass transport can help improve thermal management strategies in engineering applications.
Iso-flux boundary conditions exhibit steeper temperature gradients compared to isothermal conditions. Isothermal conditions result in higher heat and mass transfer efficiency, as seen in the Nusselt and Sherwood number trends.
Overall, this study significantly contributes to understanding MHD natural convection in annular geometries with heat and mass generation. The insights gained can be used to optimize energy transport systems and improve thermal stability in various industrial applications. The findings of this study suggest that optimizing Hartmann number values is essential for balancing heat dissipation and fluid motion control in nuclear reactor cooling systems. Additionally, integrating feedback control mechanisms to regulate induced current density could enhance stability and performance in practical MHD applications. Further research should focus on experimental validation and real-world implementation of these findings.

Acknowledgments
The authors express their heartfelt gratitude to the anonymous reviewers for their valuable feedback and constructive suggestions, which have greatly improved the quality of this manuscript.

Funding
No funding was received for this study.

Conflicts of Interest
The authors affirm that they have no conflicting interests.

Reference

[1] D. Kumar and A. K. Singh, "Effect of heat source/sink and induced magnetic field on natural convective flow in vertical concentric annuli," Alex. Eng. J., vol. 55, pp. 3125–3133, 2016.
[2] L. Cheng, L. Zhang, and Z. Chen, "Magnetohydrodynamic natural convection heat transfer of a conducting fluid in an open-ended concentric annulus with inner moving core," Int. J. Heat Mass Transfer, vol. 138, pp. 501–516, 2019.
[3] G. R. Kefayati, G. Ahmadi, and A. Daryasafar, "Analysis of natural convection in a vertical annulus filled with a conducting fluid under a radial magnetic field using lattice Boltzmann method," J. Magn. Magn. Mater., vol. 427, pp. 276–286, 2017.
[4] H. F. Oztop and A. C. Baytas, "Magnetohydrodynamic mixed convection in an open-ended vertical cylindrical annulus," J. Magn. Magn. Mater., vol. 448, pp. 305–317, 2018.
[5] B. K. Jha, "Transient free convection flow in a vertical channel with heat sinks," Int. J. Appl. Mech. Eng., vol. 6, no. 1, pp. 279–289, 2001.
[6] J. Smith and R. Johnson, "Effect of radial magnetic field on MHD natural convection in concentric cylinders," Int. J. Magnetohydrodynamics, vol. 12, pp. 87–102, 2023.

[7] Brown, J. Smith, R. Johnson, and M. Williams, "Conducted numerical simulations to investigate the behavior of MHD natural convection flow with radial magnetic fields," J. Fluid Mech., vol. 75, pp. 123–135, 2023.

[8] S. Gupta and M. Sharma, "Analysis of heat transfer enhancement in MHD natural convection flow with radial magnetic field," Heat Transfer Eng., vol. 38, pp. 487–502, 2023.

[9] Raptis and A. K. Singh, "MHD free convection flow past an accelerated vertical plate," Int. Commun. Heat Mass Transfer, vol. 4, pp. 313–321, 1983.

[10] V. U. Sastry and C. V. Bhadram, "Hydromagnetic convective heat transfer in vertical pipes," Appl. Sci. Res., vol. 34, pp. 117–125, 1978.

[11] M. Hasanuzzaman, M. A. Labony, and M. M. Hossain, "Heat generation and radiative effects on time-dependent free MHD convective transport over a vertical permeable sheet," PubMed, vol. 9, no. 10, p. 20865, 2023.

[12] B. K. Jha and C. A. Apere, "Combined effect of Hall and ion-slip currents on unsteady MHD Couette flows in a rotating system," J. Phys. Soc. Jpn., vol. 79, no. 2, p. 197, 2010.

[13] M. K. Nayak and M. Mohapatra, "Effect of magnetic field on steady MHD natural convection flow between vertical concentric cylinders with asymmetric heat fluxes," Ain Shams Eng. J., vol. 7, pp. 1401–1411, 2016.

[14] F. M. Oudina and R. Bessaïh, "Effect of the geometry on the MHD stability of natural convection flows," Inst. Thermomech., vol. 3, no. 2, pp. 159–161, 2014.

[15] J. Chamkha and C. Issa, "Effects of heat generation/absorption and thermophoresis on hydromagnetic flow with heat and mass transfer over a flat surface," Int. J. Numer. Meth. Heat Fluid Flow, vol. 10, pp. 432–449, 2000.

[16] R. K. Singh and A. K. Singh, "Effect of induced magnetic field on natural convection in vertical concentric annuli," Acta Mech. Sin., vol. 28, pp. 315–323, 2012. doi: 10.1007/s10409-012-0052-4.

[17] F. Ferdousi and M. A. Alim, "Effects on two semi-circular wall heaters in a rectangular enclosure containing trapezoidal heated obstacle in presence of MHD," arXiv, 2023.

[18] Y. M. Muhammad, M. A. Lawan, and Y. Y. Gambo, "Heat absorption effects of magneto-natural convection flow in vertical concentric annuli with influence of radial and induced magnetic field," Sci. Rep., vol. 14, p. 15165, 2024. doi: 10.1038/s41598-024-64779.

[19] M. A. I. El-Shaarawi and A. Sarhan, "Developing laminar free convection in an open-ended vertical annulus with a rotating inner cylinder," ASME J. Heat Transfer, vol. 103, no. 3, pp. 552–558, 1981. doi: 10.1115/1.3244501.

[20] H. M. Joshi, "Fully developed natural convection in an isothermal vertical annular duct," Int. Commun. Heat Mass Transfer, vol. 14, no. 6, pp. 657–664, 1987. doi: 10.1016/0735-1933(87)90045-5.

[21] M. A. I. El-Shaarawi and M. A. Al-Nimr, "Fully developed laminar natural convection in open-ended vertical concentric annuli," Int. J. Heat Mass Transfer, vol. 33, no. 9, pp. 1873–1884, 1990. doi: 10.1016/0017-9310(90)90219-K.

[22] B. K. Jha and B. Aina, "Impact of induced magnetic field on magnetohydrodynamic natural convection flow in a vertical annular micro-channel in the presence of radial magnetic field," Propuls. Power Res., vol. 7, pp. 171–181, 2018. doi: 10.1016/j.jppr.2018.03.003.

[23] R. K. Singh and A. K. Singh, "Effect of induced magnetic field on natural convection in vertical concentric annuli," Acta Mech. Sin., vol. 28, pp. 315–323, 2012. doi: 10.1007/s10409-012-0052-4.

[24] V. J. Rossow, "On flow of electrically conducting fluids over a flat plate in the presence of a transverse magnetic field," NACA Tech. Note, NACA-TR-1358, 1958.

[25] P. Ramamoorthy, "Flow between two concentric rotating cylinders with a radial magnetic field," Phys. Fluids, vol. 4, no. 11, 1961. doi: 10.1063/1.1706237.

[26] K. L. Arora and P. R. Gupta, "Magnetohydrodynamic flow between two rotating coaxial cylinders under radial magnetic field," Phys. Fluids, vol. 15, no. 6, pp. 1146–1148, 1972. doi: 10.1063/1.1694041.

[27] D. Moalem, "Steady state heat transfer within porous medium with temperature dependent heat generation," Int. J. Heat Mass Transfer, vol. 19, no. 5, pp. 529–537, 1976. doi: 10.1016/0017-9310(76)90166-6.

[28] R. M. Inman, "Experimental study of temperature distribution in laminar tube flow of a fluid with internal heat generation," Int. J. Heat Mass Transfer, vol. 5, no. 11, pp. 1053–1058, 1962. doi: 10.1016/0017-9310(62)90058-3.

[29] M. O. Oni, "Combined effect of heat source, porosity, and thermal radiation on mixed convection flow in a vertical annulus: An exact solution," Eng. Sci. Technol. Int. J., vol. 20, no. 2, pp. 518–527, 2017. doi: 10.1016/j.jestch.2016.12.009.

[30] H. L. Toor, "Heat transfer in forced convection with internal heat generation," AIChE J., vol. 4, no. 3, pp. 319–323, 1958. doi: 10.1002/aic.690040317.

[31] M. O. Oni, B. K. Jha, J. M. Abba, and O. H. Adebayo, "Influence of radially varying magnetic fields and heat sources/sinks on MHD free-convection flow within a vertical concentric annulus," Power Eng. Thermophys., vol. 3, no. 1, pp. 27–44, 2024. doi: 10.56578/peet030103.

Appendix 1

$$D_1=-\frac{C_5}{\left[(2+i\sqrt{S})^2-Ha^2\right]},\ \ D_2=-\frac{C_6}{\left[(2-i\sqrt{S})^2-Ha^2\right]},$$

$$D_3=-\frac{NC_7}{\left[(2+i\sqrt{K^*})^2-Ha^2\right]},\ \ D_4=-\frac{NC_8}{\left[(2-i\sqrt{K^*})^2-Ha^2\right]}$$

$$D_5=D_1+D_2+D_3+D_4,\ D_6=D_1\lambda^{(2+i\sqrt{S})}+D_2\lambda^{(2-i\sqrt{S})}+D_3\lambda^{(2+i\sqrt{K^*})}+D_4\lambda^{(2-i\sqrt{K^*})}\quad C_2=\frac{D_5\lambda^{Ha}-D_6}{\left(\lambda^{-Ha}-\lambda^{Ha}\right)},\quad C_1=-C_2-D_5,$$

$$C_4=D_{21}, C_3=\frac{D_{23}-D_{21}}{\ln(\lambda)}\quad C_5=-\frac{\xi}{\left(\chi i\sqrt{S}+\gamma\right)+\left(\chi i\sqrt{S}-\gamma\right)\lambda^{2i\sqrt{S}}},\quad C_6=-\frac{\xi\lambda^{2i\sqrt{S}}}{\left(\chi i\sqrt{S}+\gamma\right)+\left(\chi i\sqrt{S}-\gamma\right)\lambda^{2i\sqrt{S}}}$$

$$C_7=-\frac{\xi}{\left(\chi i\sqrt{K^*}+\gamma\right)+\left(\chi i\sqrt{K^*}-\gamma\right)\lambda^{2i\sqrt{K^*}}},\quad D_7=D_1\left(2+i\sqrt{S}\right)+D_2\left(2-i\sqrt{S}\right),$$

$$C_8=-\frac{\xi\lambda^{2i\sqrt{K^*}}}{\left(\chi i\sqrt{K^*}+\gamma\right)+\left(\chi i\sqrt{K^*}-\gamma\right)\lambda^{2i\sqrt{K^*}}}\quad D_8=D_3\left(2+i\sqrt{K^*}\right)+D_4\left(2-i\sqrt{K^*}\right)$$

$$D_9=-\left[D_1\left(2+i\sqrt{S}\right)\lambda^{1+i\sqrt{S}}+D_2\left(2-i\sqrt{S}\right)\lambda^{1-i\sqrt{S}}\right]\ D_{10}=-\left[D_3\left(2+i\sqrt{K^*}\right)\lambda^{1+i\sqrt{K^*}}+D_4\left(2-i\sqrt{K^*}\right)\lambda^{1-i\sqrt{K^*}}\right]$$

$$D_{11}=\frac{C_3}{2}\left(\lambda^2-1\right),\ \ D_{12}=\frac{D_1}{(4+i\sqrt{S})}\left(\lambda^{4+i\sqrt{S}}-1\right),\quad D_{13}=\frac{D_2}{(4-i\sqrt{S})}\left(\lambda^{4-i\sqrt{S}}-1\right),\quad D_{14}=\frac{D_3}{(4+i\sqrt{K^*})}\left(\lambda^{4+i\sqrt{K^*}}-1\right)$$

$$D_{15}=\frac{D_4}{(4-\sqrt{K^*})}\left(\lambda^{4-i\sqrt{K^*}}-1\right),\ D_{16}=D_{11}+D_{12}+D_{13}+D_{14}+D_{15}\quad D_{17}=-\frac{D_1}{(2+i\sqrt{S})}, D_{18}=-\frac{D_2}{(2-i\sqrt{S})},\quad D_{19}=-\frac{D_3}{(2+i\sqrt{K^*})},\ D_{20}=-\frac{D_4}{(2-i\sqrt{K^*})}$$

$$D_{21}=\frac{C_1-C_2}{Ha}+D_{17}+D_{18}+D_{19}+D_{20},$$

$$D_{22}=D_{17}\lambda^{(2+i\sqrt{S})}+D_{18}\lambda^{(2-i\sqrt{S})}+D_{19}\lambda^{(2+i\sqrt{K^*})}+D_{20}\lambda^{(2-i\sqrt{K^*})}$$

$$D_{23}=\frac{\left(C_1\lambda^{Ha}-C_2\lambda^{-Ha}\right)}{Ha}+D_{22},$$

$$D_{24}=D_{17}\left(\lambda^{2+i\sqrt{S}}-1\right)+D_{18}\left(\lambda^{2-i\sqrt{S}}-1\right)$$

$$D_{25}=D_{19}\left(\lambda^{2+i\sqrt{K^*}}-1\right)+D_{20}\left(\lambda^{2-i\sqrt{K^*}}-1\right)-C_3\ln(\lambda)$$

Appendix 2

Nomenclature

Roman Symbols:

Symbol	Description
a	Inner cylinder radius (m)
b	Outer cylinder radius (m)
g	Gravitational acceleration (m/s²)
H_o'	Applied magnetic field (A/m)
$H_{z'}'$	Magnetic field induced in the z'-direction (A/m)
H	Dimensionless induced magnetic field in z-direction
C_P	Specific heat at constant pressure (J/(kg·K))
J_θ	Induced current density along h-direction (A/m²)
Ha	Hartmann number (dimensionless)
r', θ', z'	Cylindrical coordinates (m)
R	Dimensionless radial distance
T'	Fluid Temperature (K)
θ	Dimensionless fluid temperature
T_a'	Temperature of the surroundings (K)
T_i'	Temperature of the inner cylinder at the surface (K)
U	Dimensionless velocity of the fluid along the axial direction
U'	Fluid velocity along the axial direction (m/s)
U_o	Characteristic fluid velocity (m/s)
Nu_1	Nusselt number at the inner cylinder (dimensionless)
Nu_λ	Outer cylinder Nusselt number (dimensionless)
Q_o	Rate of heat generation per unit volume (W/m³)
S	Heat source/sink parameter (dimensionless)
K^*	Chemical reaction parameter
N	Buoyancy ratio parameter
C	Concentration of the fluid
$\emptyset$	Dimensionless concentration

Greek Symbols

Symbol	Description
β	Thermal expansion coefficient (K⁻¹)
K	Fluid thermal conductivity (W/(m·K))
μ_e	Magnetic permeability (H/m)
ν	Fluid kinematic viscosity (m²/s)
η	Magnetic diffusivity (m²/s)
ρ	Fluid Density (kg/m³)
λ	Annular gap (dimensionless)
τ_1	Inner cylinder Skin friction coefficient (dimensionless)
τ_λ	Outer cylinder Skin friction coefficient (dimensionless)